Rotation and Translation Registration of Bandlimited Interferometric Images using a Chirp Z-Transform

Alexander S. Iacchetta[a], James R. Fienup[a], and David T. Leisawitz[b]
[a]Institute of Optics, Univ. of Rochester, 275 Hutchison Rd., Rochester, NY, USA 14627–0186
[b]NASA Goddard Space Flight Center, 8800 Greenbelt Rd., Greenbelt, MD, USA 20771–2400

ABSTRACT

Image reconstruction algorithms for wide-field spatio-spectral interferometry require knowledge of registration parameters associated with low-resolution image measurements at various baseline orientations, such that the images can be registered to within the fine resolution of the final desired image. We have developed an image registration procedure that combines a nonlinear optimization algorithm with the sub-pixel precision of chirp z-transform resampling, particularly for rotation and translation, of bandlimited images with non-radially symmetric aberrations. We show the accuracy of this image registration technique on simulated images that have a complexity comparable to scenes observed experimentally with NASA's wide-field imaging interferometry testbed. Registration to within a tenth of a pixel for translation and within three arcminutes for rotation is demonstrated at the largest simulated noise levels.

Keywords: Image registration, resampling, chirp z-transform, nonlinear optimization, double-Fourier interferometry, spatio-spectral interferometry, WIIT

1. INTRODUCTION

Image registration techniques are required in many imaging applications from tracking changes in medical images to super-sampling of under-sampled images. For the latter, accurate registration is essential for overall performance. This is also the case for wide-field spatio-spectral, or double-Fourier, interferometric imaging, which is an emerging sparse-aperture astronomical imaging technique that can be viewed as an extension of Fourier transform imaging spectroscopy. In such an interferometer, the beam from one of two physically separated collecting apertures undergoes a path delay prior to beam combination at a beamsplitter. Beam combination is followed by an imaging camera and array detector such that, if one of the beams from the two apertures were blocked, the result would be a panchromatic image of the source. The vector separation between the apertures is referred to as a baseline. For a single baseline length and orientation, images are taken for many different path delays, resulting in a single measurement cube. A spatio-spectral measurement set consists of many measurement cubes taken at various baselines. A measurement set can then be reduced to a single high-spatial-resolution, hyperspectral image using a synthesis algorithm, such as that developed by Lyon *et al*. [1, 2].

Although spatio-spectral image synthesis algorithms have been demonstrated on simulated data [1, 2], experimental effects create considerable challenges. The experimental realization that we are most concerned with is NASA's Wide-field Imaging Interferometry Testbed (WIIT), which was built for the advancement of spatio-spectral interferometry in preparation for future space-based observatories [3–13]. This state-of-the-art testbed resides in the well-controlled environment of the Advanced Interferometry and Metrology laboratory at Goddard Space Flight Center; however, despite the quality of the environment, the light source to WIIT, known as the calibrated hyperspectral image projector (CHIP) [14–16], generates heat that causes mild image motion between measurements. Even in an absolutely ideal environment free from image motion, the center of rotation would still need to be recovered in order to accurately synthesize the image measurements at various baseline angles. This is due to the fact that WIIT operates with a fixed baseline orientation, relying on rotation of the source to provide angular diversity.

In this paper we discuss a very general approach to image registration for WIIT measurements. We will demonstrate the accuracy of the image registration process on simulated WIIT measurements for several baselines lengths and orientations. The center of rotation and image translations are degenerate parameters, so we will take the fast Fourier transform (FFT) convention for the DC pixel as the center of rotation. This is particularly useful because we implement image resampling with a chirp z-transform (CZT) algorithm, which itself is computed using multiple FFTs. The image registration algorithm as a whole, including the CZT algorithm and its incorporation into an image registration procedure, is included in Sec. 2. Sec. 3 describes spatio-spectral interferometric measurements, including how to

Optical and Infrared Interferometry and Imaging V, edited by Fabien Malbet, Michelle J. Creech-Eakman, Peter G. Tuthill, Proc. of SPIE Vol. 9907, 99073G
 · doi: 10.1117/12.2232178

preprocess the data prior to image registration. The results of image registration on simulated data are shown in Sec. 4, and some concluding remarks and future work are given in Sec. 5.

2. IMAGE REGISTRATION VIA NONLINEAR OPTIMIZATION

We first describe the CZT algorithm that we use to perform image resampling, including rotations and translations, as well as possible up-sampling or down-sampling. We will then discuss nonlinear optimization and how it facilitates image registration through the CZT algorithm.

2.1 Chirp z-transform resampling

CZT resampling is not a new idea, and has been applied to a variety of topics, including blind deconvolution, phase retrieval, and super-sampling [17, 18]. Not all implementations of the CZT algorithm are equivalent; for example, we have chosen to employ the 2D CZT rotation algorithm formulated by Myagotin and Vlasov [19] instead of successive 1D CZT operations [17, 18]. We will derive the 2D CZT rotation algorithm here in a style similar to that of Myagotin and Vlasov [19]; although, the factorization that facilitates this 2D method was first published by Tong and Cox [20].

Let G_{mn} be the discrete Fourier transform (DFT) of the image g_{xy} we want to rotate. Now consider the inverse DFT of G_{mn}:

$$\begin{aligned} g_{xy} &= \sum_{m,n=-\frac{N}{2}}^{\frac{N}{2}-1} G_{mn} \exp\left[i\frac{2\pi}{N}(mx+ny) \right] \\ &= \sum_{m,n=0}^{N-1} G_{\left(m-\frac{N}{2}\right)\left(n-\frac{N}{2}\right)} \exp\left\{ i\frac{2\pi}{N}\left[\left(m-\frac{N}{2}\right)x + \left(n-\frac{N}{2}\right)y \right] \right\}, \end{aligned} \tag{1}$$

where we have assumed G_{mn} is a square array. $G_{(m-N/2)(n-N/2)}$ is equivalent to performing an fftshift on G_{mn}. Explicitly discretize the x- and y-dimensions: $(x,y) = (r,s)\Delta_{xy}$, where $r,s = 0,...,R-1$, and Δ_{xy} is the pixel spacing and is assumed to be equal in both dimensions. If we rotate the discretized x- and y-coordinates about the point (x_0, y_0) by an angle θ, the rotated coordinates become

$$x' = (\Delta_{xy} r - x_0)\cos\theta - (\Delta_{xy} s - y_0)\sin\theta + x_0, \tag{2}$$

$$y' = (\Delta_{xy} r - x_0)\sin\theta + (\Delta_{xy} s - y_0)\cos\theta + y_0. \tag{3}$$

Replacing (x,y) with (x',y') in Eq. (1), we obtain

$$g_{x'y'} = g'_{rs} = \sum_{m,n=0}^{N-1} G_{\left(m-\frac{N}{2}\right)\left(n-\frac{N}{2}\right)} \exp\left\{ i\frac{2\pi}{N}\left[\left(m-\frac{N}{2}\right)x' + \left(n-\frac{N}{2}\right)y' \right] \right\}. \tag{4}$$

Using Eqs. (2) and (3), we can expand Eq. (4) to take the following form:

$$\begin{aligned} g'_{rs} &= \exp\left\{ -i\pi\left[(\Delta_{xy} r - x_0)(\cos\theta + \sin\theta) + (\Delta_{xy} s - y_0)(\cos\theta - \sin\theta) \right] \right\} \\ &\times \sum_{m,n=0}^{N-1} G_{\left(m-\frac{N}{2}\right)\left(n-\frac{N}{2}\right)} \exp\left\{ i\frac{2\pi}{N}\left[\left(m-\frac{N}{2}\right)x_0 + \left(n-\frac{N}{2}\right)y_0 \right] \right\} \\ &\times \exp\left\{ -i\frac{2\pi}{N}\left[(x_0\cos\theta - y_0\sin\theta)m + (x_0\sin\theta + y_0\cos\theta)n \right] \right\} \\ &\times \exp\left\{ i\frac{2\pi\Delta_{xy}}{N}\left[\cos\theta(mr+ns) + \sin\theta(nr-ms) \right] \right\}. \end{aligned} \tag{5}$$

In order to take advantage of the CZT algorithm, we will need to write Eq. (5) in the form of a convolution; to do this, we adopt the expansion first published by Tong and Cox [20]:

$$\begin{aligned}(mr+ns) &= -(s-m)(r-n)+mn+rs \\ 2(nr-ms) &= (s-m)^2-(r-n)^2+\left(n^2-m^2\right)+\left(r^2-s^2\right).\end{aligned} \tag{6}$$

Eq. (6) allows us to rewrite Eq. (5) in the form of a 2D CZT. After rearranging and grouping terms, Eq. (5) becomes

$$g'_{rs} = A_{rs}\sum_{m,n=0}^{N-1} B_{mn}G_{\left(m-\frac{N}{2}\right)\left(n-\frac{N}{2}\right)}H_{(s-m)(r-n)}\,, \tag{7}$$

where

$$\begin{aligned}A_{rs} &= \exp\left[-i2\pi\alpha rs - i\pi\beta\left(r^2-s^2\right)\right] \\ &\times\exp\left\{-i\pi\left[\left(\Delta_{xy}r-x_0\right)(\cos\theta+\sin\theta)+\left(\Delta_{xy}s-y_0\right)(\cos\theta-\sin\theta)\right]\right\},\end{aligned} \tag{8}$$

$$\begin{aligned}B_{mn} &= \exp\left[-i2\pi\alpha mn - i\pi\beta\left(n^2-m^2\right)\right]\exp\left\{i\frac{2\pi}{N}\left[\left(m-\frac{N}{2}\right)x_0+\left(n-\frac{N}{2}\right)y_0\right]\right\} \\ &\times\exp\left\{-i\frac{2\pi}{N}\left[\left(x_0\cos\theta-y_0\sin\theta\right)m+\left(x_0\sin\theta+y_0\cos\theta\right)n\right]\right\},\end{aligned} \tag{9}$$

$$H_{mn} = \exp\left[i2\pi\alpha mn + i\pi\beta\left(n^2-m^2\right)\right], \tag{10}$$

and

$$(\alpha,\beta) = -\frac{\Delta_{xy}}{N}(\cos\theta,\sin\theta)\,. \tag{11}$$

Although Eq. (7) appears as a regular convolution, it is important to point out that, the way the equation is written, the convolution kernel H_{mn}, or equivalently the input array G_{mn}, must have its axes swapped prior to performing the convolution. Fortunately, this can be solved using a simple transpose operation (as opposed to transpose-conjugate).

A sub-pixel image shift prior to the rotation can be performed by adding another linear phase term to B_{mn}, or directly to the input array G_{mn}, which does not change the computational complexity of the CZT rotation algorithm. In addition to rotation and translation, this same algorithm is capable of changing the sampling rate in the output plane with the variable Δ_{xy}, which is possible because the desired sample spacing in the output plane is arbitrary. This means that with the addition of padding and cropping operations, this CZT algorithm can also simulate changes in the magnification of an optical system, where $\Delta_{xy}<1$ increases the number of samples in the output array compared to the input array by a factor of Δ_{xy}. It should be noted that the arguments of the 2D CZT algorithm in Eq. (7) are subject to the same padding requirements as the 1D CZT algorithm as described by Rabiner *et al.* [21] and Baily and Swarztrauber [22]. For two dimensions, the padding considerations are described by Jurling and Fienup [23], who also describe how the 2D CZT can be performed with three FFTs and that a prudent choice of padding size can improve the performance of the algorithm. We also note that it is possible to incorporate various system transfer functions in the spatial frequency domain as part of the CZT algorithm, allowing simulations of system aberrations, pixel transfer functions, or atmospheric turbulence.

Rotation via the CZT algorithm is equivalent to using 2D sinc interpolation to perform the shift, rotation and resampling but with lower computational complexity [17, 21, 22]. Due to the frequency-based nature of this method, it works best for bandlimited images in order to prevent the algorithm from inducing unwanted aliasing; however, this problem can be overcome by paying special attention to sampling and zero-padding throughout the computation. In total, the CZT rotation algorithm requires four FFTs, typically of a larger size than the original image to be rotated. Accordingly, the computation time for this rotation algorithm is much greater than for bilinear resampling, but CZT resampling provides more accurate rotations than the bilinear resampling method. We now turn our attention toward incorporating the CZT algorithm described in this section into an image registration algorithm through nonlinear optimization of the registration parameters.

2.2 Nonlinear optimization

In this section we use nonlinear optimization to perform image registration, employing the rotation and translation algorithm from Sec. 2.1. Assume that we have a set of *K* measured images $\tilde{g}_k(r,s)$ to be registered to a single reference image $f(r,s)$. Starting with *K* estimates for the image registration parameters, particularly rotation and translation, we apply the CZT resampling algorithm from Sec 2.1 *K* times so that we now have *K* rotated and shifted images $\hat{f}_k(r,s;\theta_k,x_{0,k},y_{0,k})$, which we can compare to the measurements, where the hat denotes that the variable is an estimate for the measured image.

Now that we have a forward model, optimization algorithms require that we have a scalar error metric to determine how well the simulated images predicted with the forward model compare to the measured images. We have chosen a gain and bias invariant normalized mean square error metric (NMSE) between the predicted images $\hat{f}_k(r,s;\theta_k,x_{0,k},y_{0,k})$ and measured images $\tilde{g}_k(r,s)$ to promote data consistency [24]:

$$E=\frac{1}{K}\sum_{k=1}^{K}\frac{\sum_{r,s}w_k(r,s)\left[\sigma_k\hat{f}_k(r,s;\theta_k,x_{0,k},y_{0,k})+\varepsilon_k-\tilde{g}_k(r,s)\right]^2}{\sum_{r,s}w_k(r,s)\tilde{g}_k^2(r,s)}, \tag{12}$$

where σ_k is the signal gain, ε_k is the signal bias, and $w_k(r,s)$ is a weighting function that can be used to emphasize particular pixels or ignore dead pixels. We used the weighting functions to mask out the areas in $\hat{f}_k(r,s;\theta_k,x_{0,k},y_{0,k})$ where $f(r,s)$ did not contribute any information, often in the corners of the transformed images. Given a particular measurement and model image, the optimal gain and bias can be computed independently of other parameters, and they are helpful for mitigating detector-induced errors for experimental datasets. Because we are only concerned with image registration and need not optimize over pixel values directly, we did not incorporate any regularizing metrics with our data consistency metric. It is worth noting that it is possible to register the images jointly, as suggested by Eq. (12), or individually for each $\tilde{g}_k(r,s)$. We chose to register the images jointly in order to avoid recalculating intermediate variables required for the CZT resampling algorithm from Sec. 2.1.

Nonlinear optimization algorithms require one to supply a gradient of the error metric with respect to all optimization variables; in this case, we are optimizing over rotation angles and image translations. Instead of deriving analytic expressions for the gradients, we employed algorithmic differentiation, which is a formulaic method for computing analytic gradients in a step-by-step fashion where every computation in the forward model has a corresponding step in the gradient model. By breaking up the gradient computation into small pieces, it becomes much less daunting to compute analytic gradients for complicated forward models. The idea of algorithmic differentiation has recently been made more accessible for image reconstruction and phase retrieval by Jurling and Fienup [25]. We have followed their formulation of algorithmic differentiation in order to compute the required gradients. The nonlinear optimization algorithm we utilized in our simulations was the limited-memory Broyden-Fletcher-Goldfarb-Shanno algorithm with bounds (L-BFGS-B) from the SciPy package for the Python computing language, although we did not impose any bounds on the optimization variables for image registration. Various stopping criteria are allowed and are ultimately problem dependent. We chose to set a tolerance of 10^{-8} on the decrease in the value of the error metric between iterations, corresponding to about a 0.01% decrease in the error metric for the majority of cases presented in this paper.

3. WIDE-FIELD SPATIO-SPECTRAL INTERFEROMETRIC SIMULATIONS

This section describes the simulated dataset and how the data are preprocessed before applying the image registration algorithm. The intricacies of implementing the simulations are beyond the scope of this paper and will be the topic of a future paper. For a single vector baseline of the interferometer, many image measurements are taken while scanning the path delay between the arms of the interferometer, resulting in a single measurement cube. If we assume that the interferometer's apertures are identical so that they have the same aberrations, a measurement cube can be represented by [2]

$$I_{meas}(\vec{\theta},\vec{B},L)=I_1(\vec{\theta})\pm\int_0^{\infty}\int_{-1}^{1}p_{1,1}(\vec{\theta}-\vec{\alpha};\kappa)S_s(\vec{\alpha};\kappa)\sin\left[2\pi\kappa(\vec{\alpha}\cdot\vec{B}+L)\right]d^2\vec{\alpha}d\kappa, \tag{13}$$

where

$$I_1(\vec{\theta}) = \int_0^{\infty} \int_{-1}^{1} p_{1,1}(\vec{\theta} - \vec{\alpha}; \kappa) S_s(\vec{\alpha}; \kappa) d^2\vec{\alpha} d\kappa, \tag{14}$$

$p_{1,1}(\vec{\theta};\kappa)$ is the point spread function (PSF) of either aperture function independently, $S_s(\vec{\alpha};\kappa)$ is the spectral density of the source, $\vec{B}$ is the vector baseline, L is the optical path difference between the arms of the interferometer, κ is the spectroscopy convention for wavenumber (the inverse of the wavelength), $\vec{\alpha}$ is the direction cosine of the source position relative to the line-of-sight of the interferometer, and $\vec{\theta}$ is the angular position of the image pixels relative to the optical axis of the imaging system within the interferometer. An entire dataset, comprised of many measurement cubes, is generated by repeating the measurement process at various vector baselines.

We preprocessed the measurement cubes by taking the average over the delay dimension, which is a method of approximating Eq. (14) from Eq. (13), and performed image registration using the result. Due to delay-line sampling, noise, and other detector effects, Eq. (14) cannot be recovered exactly but can be well approximated, resulting in averaged images that are very weakly dependent on $\vec{B}$. In this sense, the images to be registered are not exactly the same but are derived from the same underlying high-spatial-resolution object. In fact, if the PSF is not radially symmetric, the images to be registered can be significantly different because rotation occurs prior to application of the PSF. The PSF in our simulations is similar to that observed in WIIT and does not have perfect rotational symmetry. The images in Eq. (13) and (14) are bandlimited by the diameters of the input apertures, and WIIT is designed to be at least Nyquist sampled according to the diameter of a single aperture. Details of WIIT's optical parameters and source capabilities can be found in other publications [3–13]. A typical WIIT datacube contains between two and three thousand images, one for each of the sampled delay positions *L*, so the act of preprocessing reduces the standard deviation of the noise in the average of Eq. (13) by about a factor of 50.

The underlying hyperspectral image that we used for simulations is similar to a Hubble deep-field image but was based on a model of the far infrared sky. After passing through the interferometer's optical system, the image of the scene becomes blurred, due to the modest aperture size, so that it is difficult to discern the many galaxies from the diffuse background emission and light from nearby galaxies. We also injected point-like reference sources outside of the core of the deep-field scene that will eventually be useful for calibration. This scene was developed to probe the efficacy of spatio-spectral interferometry with WIIT, and is currently being used to take measurements with WIIT [26]. The simulated dataset we used consisted of one datacube that served as a reference image whose rotation and translations were known to be identically zero, while the rest of the dataset consisted of 10 datacubes whose translations were unknown and drawn from a uniform distribution that allowed a maximum image shift of 2.5 pixels in either dimension. The rotations of the 10 datacubes were assumed known to the nearest half a degree, where the noise added to the rotation angles were also drawn from a uniform distribution. Fig. 1(b) is the result of averaging Eq. (13) for the reference image in our simulations.

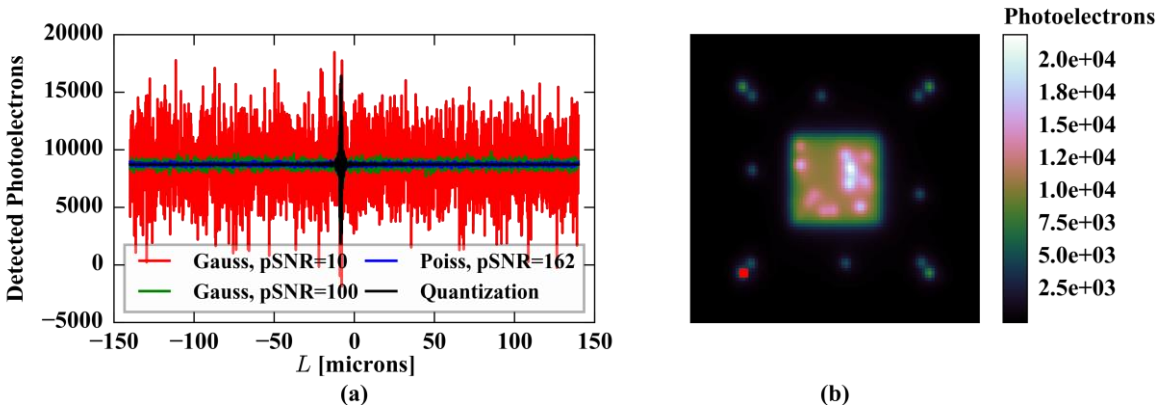

Figure 1. Example of simulated WIIT data. (a) The fringes at a particular pixel of the datacube for four of the five noise realizations used in this paper, and (b) the average along the delay dimension, where the highlighted pixel in the lower left corner is the location of the fringes in (a).

We investigated how various noise models in the datacube measurements, Eq. (13), affect registration accuracy. The first noise model only takes into account the effect of detector quantization, which also limits the overall dynamic range. WIIT has a high-quality 16-bit CCD camera with unity gain. We assumed that the peak value of the entire dataset was 40% of the 16-bit maximum, or 26,214 counts, for all results shown in this paper. This is also the value we use when referring to peak signal-to-noise (pSNR) values, which, for Poisson noise, is then $\sqrt{26,214} \simeq 162$. In conjunction with Poisson noise and quantization noise, we added different levels of read noise, where the pSNRs for read noise were 100, 10, and 1. In all, we tried 5 different noise combinations: quantization noise only, quantization noise and Poisson noise, and the combination of quantization noise, Poisson noise and read noise for the 3 different read noise levels. Fig. 1(a) shows the fringes of Eq. (13) as a function of L at a particular pixel for various noise levels, excluding the read noise case with a pSNR of 1 because it would make it more difficult to identify the fringe near the center of the plot. Five images from the dataset are displayed in Fig. 2 for the various noise levels. To show more dim background detail, all subsequent images have been stretched to the 0.3 power after setting negative values to zero.

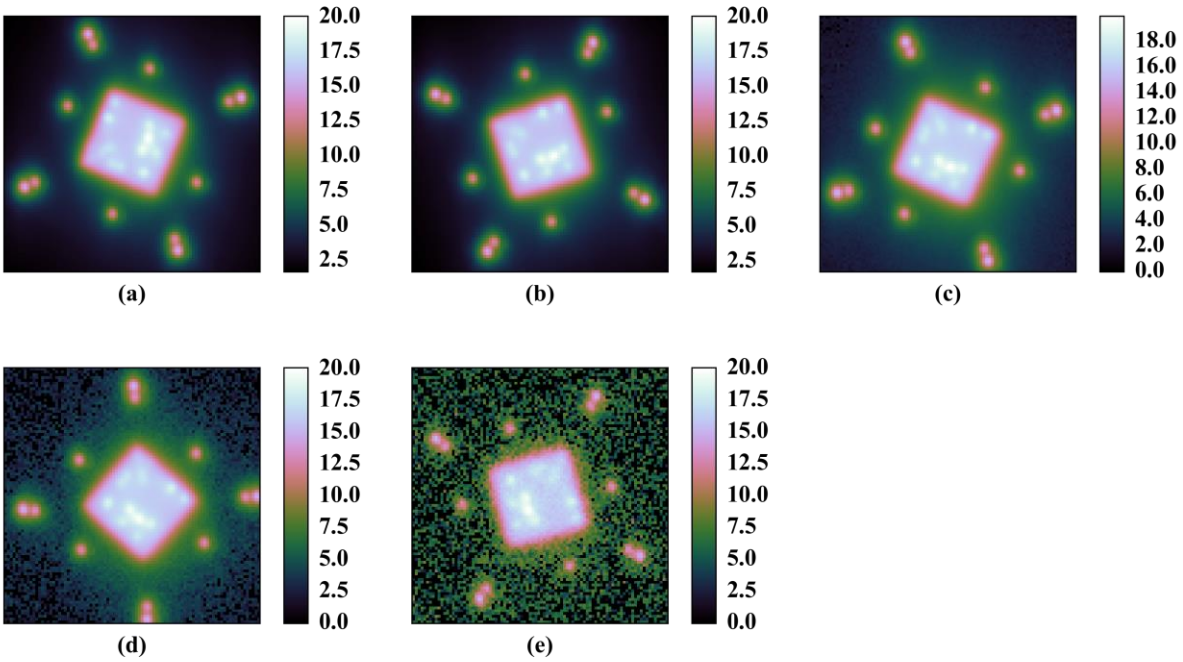

Figure 2. Five images from the dataset with different rotations and translations, stretched to the 0.3 power after setting negative values to zero. Images shown with increasing noise levels of (a) quantization only, (b) quantization and Poisson noise, and (c) through (d) have quantization noise, Poisson noise, and Gaussian read noise with pSNR values of 100, 10, and 1, respectively.

4. IMAGE REGISTRATION RESULTS

The initial values of the registration parameters are important because nonlinear optimization routines can be prone to local minima issues that can prevent the algorithm from finding the global minimum. The rotations, as mentioned in Sec. 3, were known a priori to the nearest half a degree. The initial translation values were assumed to be zero. Another source of error comes from noise in the reference image, which is assumed to come from the overall dataset, even though it is considered separate from the dataset for the purposes of this paper. In order to reduce the impact of noise in the reference image, we obtained a new estimate of the reference image after performing one run of the registration process by transforming the entire dataset to the same orientation as the original reference image and taking the average of the transformed images. This provided a new, less noisy estimate of the reference image with which we performed a second round of registration. The original reference image is shown in Fig. 3 for all of the various noise levels, and the updated reference images are displayed in Fig. 4.

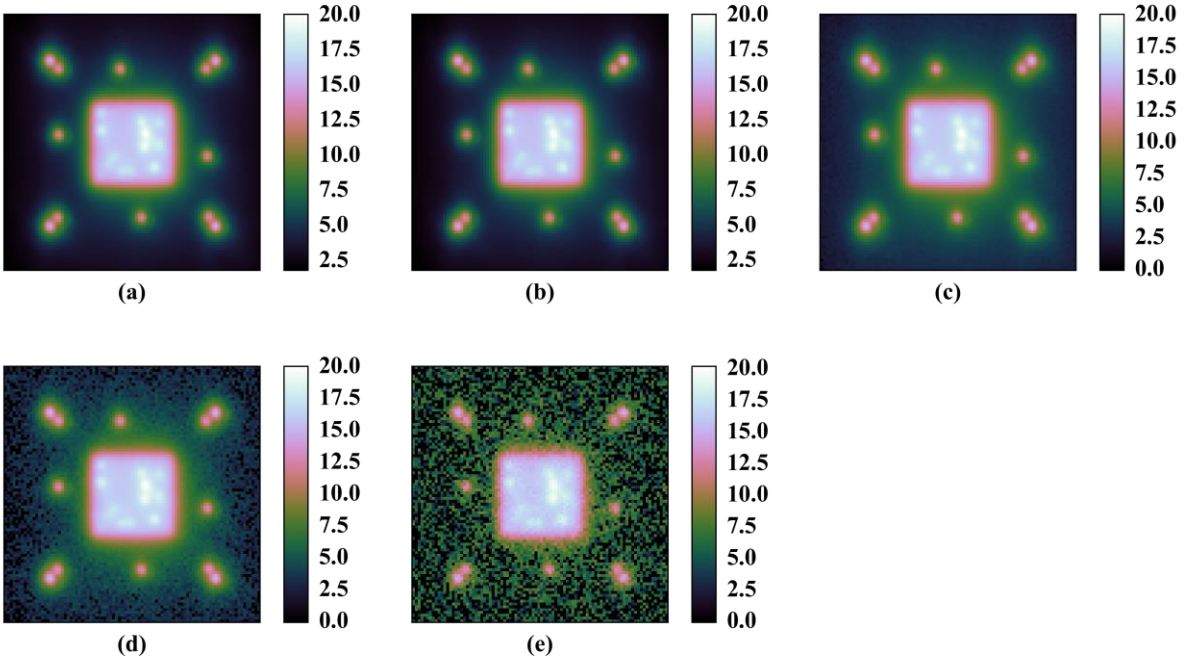

Figure 3. Reference images, stretched to the 0.3 power after setting negative values to zero, for increasing noise levels of (a) quantization only, (b) quantization and Poisson noise, and (c) through (d) have quantization noise, Poisson noise, and Gaussian read noise with pSNR values of 100, 10, and 1, respectively.

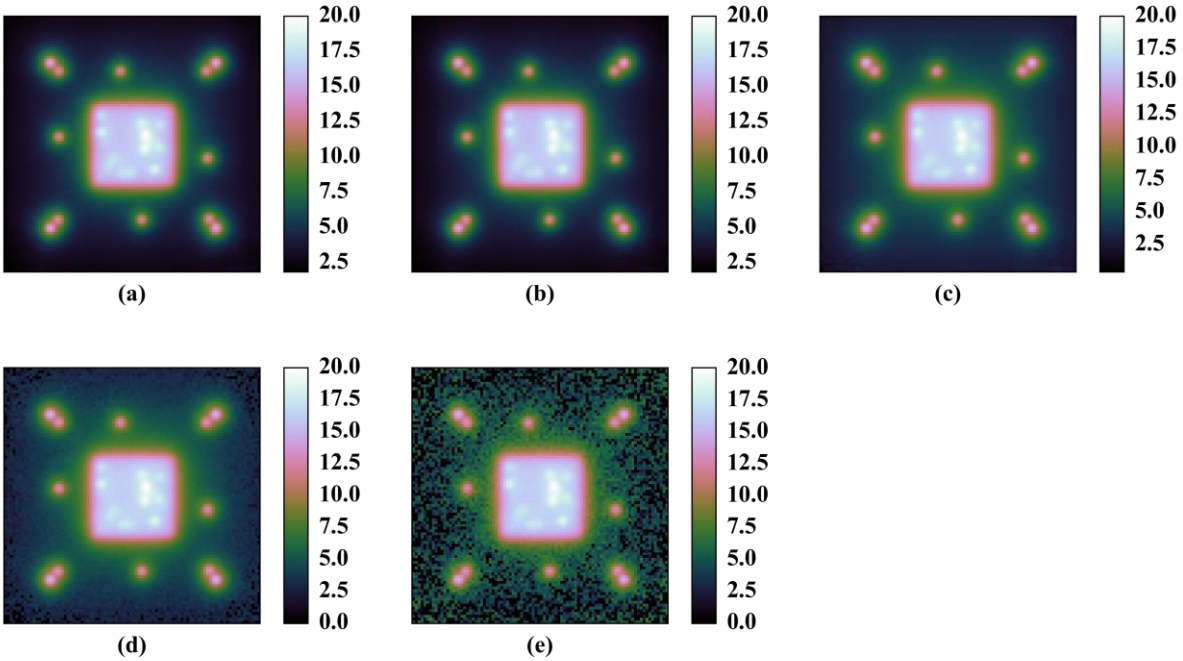

Figure 4. Reference images, with negative values set to zero and stretched to the 0.3 power, after they have been updated using the images from the registered dataset.

For quality assessment we computed both the mean absolute deviation (*MAD*) from the truth and the standard deviation (*StD*) from the truth:

$$MAD = \frac{1}{K}\sum_{k}^{K}\left|\hat{\phi}_k - \phi_t\right|, \tag{15}$$

$$StD = \sqrt{\frac{1}{K}\sum_{k}^{K}\left(\hat{\phi}_k - \phi_t\right)^2}, \tag{16}$$

where $\hat{\phi}_k$ is the estimate variable ϕ in the *k*th image, and ϕ_t is the truth value of the variable. Tables 1 and 2 show the results for the two applications of the registration algorithm, where Table 2 values were obtained after computing a new estimate of the reference image by averaging over the dataset. The translation error is for both x and y translations together.

Table 1. Results of image registration using the initial reference image for all of the noise levels, where the final error metric value is provided along with the mean absolute deviations and standard deviations for the translation and rotation parameters.

	Final NMSE	**Translation Errors (pixels)**		**Rotation Errors (degrees)**	
	E	*MAD*	*StD*	*MAD*	*StD*
Quantization Only	1.64e–03	8.60e–02	1.04e–01	6.67e–03	7.15e–03
Quantization + Poisson	1.64e–03	8.60e–02	1.04e–01	6.55e–03	7.02e–03
Quantization + Poisson + Read Noise (pSNR=100)	1.65e–03	8.60e–02	1.05e–01	6.40e–03	6.94e–03
Quantization + Poisson + Read Noise (pSNR=10)	1.94e–03	8.54e–02	1.04e–01	4.15e–03	4.98e–03
Quantization + Poisson + Read Noise (pSNR=1)	3.28e–02	8.29e–02	9.73e–02	5.44e–02	6.78e–02

Table 2. Results of image registration using the updated reference image for all of the noise levels, where the final error metric value is provided along with the mean absolute deviations and standard deviations for the translation and rotation parameters.

	Final NMSE	**Translation Errors (pixels)**		**Rotation Errors (degrees)**	
	E	*MAD*	*StD*	*MAD*	*StD*
Quantization Only	5.36e–04	8.34e–02	1.01e–01	2.24e–03	3.40e–03
Quantization + Poisson	5.36e–04	8.34e–02	1.01e–01	2.20e–03	3.35e–03
Quantization + Poisson + Read Noise (pSNR=100)	5.38e–04	8.35e–02	1.02e–01	2.17e–03	3.20e–03
Quantization + Poisson + Read Noise (pSNR=10)	6.82e–04	8.29e–02	1.01e–01	2.31e–03	2.84e–03
Quantization + Poisson + Read Noise (pSNR=1)	1.50e–02	8.00e–02	9.37e–02	3.37e–02	4.34e–02

Tables 1 and 2 reveal some interesting information about the registration technique. First, the translation registration results appear to be virtually unaffected by the noise models, and there is only a slight improvement after updating the reference image, resulting in registrations accurate to within a tenth of a pixel. The apparent drop in both the *MAD* and

StD for translation at the higher noise levels is insignificant because the standard deviations of the *MAD* calculations are about half the *MAD* values themselves. On the other hand, the rotation registration accuracy begins to degrade at the highest noise level, and there is typically a significant improvement in the registration accuracy after updating the reference image. Even at the highest noise level, we still managed to recover the rotation angles to within 3 arcminutes.

In addition to simulating the WIIT optical system, we simulated a dataset where the optical system was assumed to be free of all aberrations except defocus. Although we will not be able to make measurements from an interferometer with such an ideal optical system, we can still learn from investigating an optical system with a radially symmetric PSF. For this idealized dataset, the registration accuracy for translation improved by as much as a factor of 50, while the accuracy of the rotation angle improved by a factor of 5. This suggests that the algorithm is impacted more by model mismatch, meaning that the images are not identical after rotating to the same orientation, than by noise. One can get an understanding of the model mismatch by looking at the NMSE values for the quantization-only case, which we found to be about two orders of magnitude smaller for the case of radially symmetric aberrations. We suspect that it might be possible to improve the registration accuracy by incorporating knowledge of the system's aberrations without much additional computation because it is easy to include transfer functions into the CZT algorithm described in Sec. 2.1.

5. CONCLUSION AND FUTURE WORK

We have demonstrated the performance of an image registration algorithm for both rotation and translation using a CZT algorithm to perform resampling and nonlinear optimization to solve for the unknown registration parameters. Although this technique was developed for registering spatio-spectral interferometric images as a precursor to image synthesis, this technique is very general and could be a viable approach for many other imaging applications where rotation and translation between similar images is unknown. With careful consideration to image sampling, this procedure could also be applied to images that are under-sampled with respect to the Nyquist criterion for imaging, and in that case, can even be used to perform simultaneous super-resolution and image registration. The technique described in this paper could be improved by incorporating knowledge of the system aberrations, as suggested at the end of Sec. 4, which will be the focus of future work.

Acknowledgements

This work was supported by a NASA Space Technology Research Fellowship.

References

[1] Lyon, R. G., S. A. Rinehart, D. T. Leisawitz, and N. Memarsadeghi, "Wide-field imaging interferometry testbed (WIIT): Image construction algorithms," Proc. SPIE 7013, 70131M (2008).

[2] Lyon, R. G., D. T. Leisawitz, S. A. Rinehart, N. Memarsadeghi, and E. J. Sinukoff, "Wide-field imaging interferometry spatial-spectral image synthesis algorithms," Proc. SPIE 8445, 84450B (2012).

[3] Leisawitz, D. T., B. J. Frey, D. B. Leviton, A. J. Martino, W. L. Maynard, L. G. Mundy, S. A. Rinehart, S. H. Teng, and X. Zhang, "Wide-field imaging interferometry testbed I: purpose, testbed design, data, and synthesis algorithms," Proc. SPIE 4852, 255–267 (2003).

[4] Rinehart, S. A., B. J. Frey, D. T. Leisawitz, D. B. Leviton, A. J. Martino, W. L. Maynard, L. G. Mundy, S. H. Teng, and X. Zhang, "Wide-field imaging interferometry testbed II: implementation, performance, and plans," Proc. SPIE 4852, 674–684 (2003).

[5] Leviton, D. B., B. J. Frey, D. T. Leisawitz, A. J. Martino, W. L. Maynard, L. G. Mundy, S. A. Rinehart, S. H. Teng, and X. Zhang, "Wide-field imaging interferometry testbed 3: metrology subsystem," Proc. SPIE 4852, 827–838 (2003).

[6] Rinehart, S. A., J. T. Armstrong, B. J. Frey, J. Kirk, D. T. Leisawitz, D. B. Leviton, L. W. Lobsinger, R. G. Lyon, A. J. Martino, T. A. Pauls, L. G. Mundy, and E. Sears, "The wide-field imaging interferometry testbed: II. Characterization and calibration," Proc. SPIE 5491, 1790–1801 (2004).

[7] Thompson, A. K., A. J. Martino, S. A. Rinehart, D. T. Leisawitz, B. J. Frey, and D. B. Leviton, "Optical modeling of the wide-field imaging interferometry testbed," Proc. SPIE 6268, 62682R (2006).

[8] Rinehart, S. A., J. T. Armstrong, B. J. Frey, J. Jung, J. Kirk, D. T. Leisawitz, D. B. Leviton, R. G. Lyon, A. J. Martino, T. A. Pauls, L. G. Mundy, and A. K. Thompson, "The wide-field imaging interferometry testbed: recent results," Proc. SPIE 6268, 626836 (2006).

[9] Rinehart, S. A., J. T. Armstrong, B. J. Frey, J. Jung, J. Kirk, D. T. Leisawitz, D. B. Leviton, R. G. Lyon, S. F. Maher, A. J. Martino, and T. A. Pauls, "The wide-field imaging interferometry testbed: enabling techniques for high angular resolution astronomy," Proc. SPIE 6687, 66870F (2007).
[10] Leisawitz, D. T., A. J. Martino, A. K. Thompson, S. A. Rinehart, and B. J. Frey, "An optical model of the wide-field imaging interferometry testbed," Proc. SPIE 6687, 66870J (2007).
[11] Rinehart, S. A., D. T. Leisawitz, B. J. Frey, R. G. Lyon, S. F. Maher, and N. Memarsadeghi, "The wide-field imaging interferometry testbed (WIIT): recent progress and results," Proc. SPIE 7013, 70132S (2008).
[12] Rinehart, S. A., D. T. Leisawitz, M. R. Bolcar, K. M. Chaprnka, R. G. Lyon, S. F. Maher, N. Memarsadeghi, E. J. Sinukoff, and E. Teichman, "Recent progress in wide-field imaging interferometry," Proc. SPIE 7734, 77342D (2010).
[13] Leisawitz, D. T., M. R. Bolcar, R. G. Lyon, S. F. Maher, N. Memarsadeghi, S. A. Rinehart, and E. J. Sinukoff, "Developing wide-field spatio-spectral interferometry for far-infrared space applications," Proc. SPIE 8445, 84450A (2012).
[14] Bolcar, M. R., D. T. Leisawitz, S. F. Maher, and S. A. Rinehart, "Demonstration of the Wide-field Imaging Interferometer Testbed using a Calibrated Hyperspectral Image Projector," Proc. SPIE 8445, 84452D (2012)
[15] Rice, J. P., S. W. Brown, B. C. Johnson, and J. E. Neira, "Hyperspectral image projectors for radiometric applications," *Metrologia* **43**, S61–S65 (2006).
[16] Brown, S. W., J. P. Rice, J. E. Neira, R. R. Bousquet, and B. C. Johnson, "Hyperspectral image projector for advanced sensor characterization," Proc. SPIE 6296, 629602 (2006).
[17] Granrath, D., and J. Lersch, "Fusion of images on affine sampling grids," J. Opt. Soc. Am. A 15(4), 791–801 (1998).
[18] Gerwe, D. R., B. Eucker, C. Luna, and B. Calef, "Diversity image restoration with dynamically changing magnification, rotation, and translation," AMOS Technical Paper, (2007).
[19] Myagotin, A. V., and E. V. Vlasov, "Efficient implementation of the image rotation method using chirp z-transform," Pattern Recog. Image Anal. 24(1), 57–62 (2014).
[20] Tong, R., and R. W. Cox, "Rotation of NMR images using the 2D chirp-z transform," Magn. Resonance Med. 41(2), 253–256 (1999).
[21] Rabiner, L. R., R. W. Schafer, and C. M. Rader, "The chirp z-transform algorithm and its applications," Bell Syst. Tech. J. 48(3), 1249–1292 (1969).
[22] Bailey, D. H., and P. N. Swarztrauber, "The fractional Fourier transform and applications," SIAM Review 33(3), 389–404 (1991).
[23] Jurling, A. S., and J. R. Fienup, "Phase retrieval with unknown sampling factors via the two-dimensional chirp z-transform," J. Opt. Soc. Am. A 31(9), 1904–1911 (2014).
[24] Thurman, S. T., and J. R. Fienup, "Phase retrieval with signal bias," J. Opt. Soc. Am. A 26(4), 1008–1014 (2009).
[25] Jurling, A. S., and J. R. Fienup, "Applications of algorithmic differentiation to phase retrieval algorithms," J. Opt. Soc. Am. A 31(7), 1348–1359 (2014).
[26] Leisawitz, D. T., R. Juanola-Parramon, M. R. Bolcar, J. R. Fienup, A. S. Iacchetta, S. F. Maher, and S. A. Rinehart, "Recent experiments conducted with the Wide-field Imaging Interferometry Testbed (WIIT)," Proc. SPIE *Astronomical Telescopes + Instrumentation*, 9907–29 (2016).